Electron Doping a Kagome Spin Liquid

Z. A. Kelly,[1,2] M. J. Gallagher,[1] and T. M. McQueen[1,2,3,*]
[1]*Department of Chemistry, The Johns Hopkins University, Baltimore, Maryland 21218, USA*
[2]*Institute for Quantum Matter, Department of Physics and Astronomy, The Johns Hopkins University, Baltimore, Maryland 21218, USA*
[3]*Department of Materials Science and Engineering, The Johns Hopkins University, Baltimore, Maryland 21218, USA*

(Received 17 May 2016; revised manuscript received 25 August 2016; published 13 October 2016)

Herbertsmithite, $ZnCu_3(OH)_6Cl_2$, is a two-dimensional kagome lattice realization of a spin liquid, with evidence for fractionalized excitations and a gapped ground state. Such a quantum spin liquid has been proposed to underlie high-temperature superconductivity and is predicted to produce a wealth of new states, including a Dirac metal at $1/3$ electron doping. Here, we report the topochemical synthesis of electron-doped $ZnLi_xCu_3(OH)_6Cl_2$ from $x = 0$ to $x = 1.8$ (3/5 per Cu^{2+}). Contrary to expectations, no metallicity or superconductivity is induced. Instead, we find a systematic suppression of magnetic behavior across the phase diagram. Our results demonstrate that significant theoretical work is needed to understand and predict the role of doping in magnetically frustrated narrow band insulators, particularly the interplay between local structural disorder and tendency toward electron localization, and pave the way for future studies of doped spin liquids.

DOI: 10.1103/PhysRevX.6.041007 Subject Areas: Condensed Matter Physics, Magnetism

For decades, the resonance valance bond (RVB), or quantum spin-liquid, state has been theorized to be an intricate part of the mechanism for high-temperature superconductivity [1,2]. One geometrically frustrated system, herbertsmithite [Fig. 1(a)], is considered an ideal spin two-dimensional liquid candidate due to its perfectly ordered kagome lattice of $S = 1/2$ copper ions, antiferromagnetic interactions with $J \approx -200$ K, strong evidence for fractional spin excitations by neutron scattering, and, most recently, convincing indications of a gapped spin-liquid ground state by oxygen-17 NMR [3–8]. All of these factors suggest herbertsmithite is the realization of a quantum spin liquid. Recent predictions expanded upon Anderson's theory in density functional theory calculations of electron-doped herbertsmithite, $M_xZn_{1-x}Cu_3(OH)_6Cl_2$, where Ga^{3+} or other aliovalent metals replace zinc [9,10]. A trivalent substitution introduces electrons into the material, raising the Fermi level to the Dirac points at $x = 1$, and giving rise to a rich phase diagram spanning from a frustrated RVB spin liquid ($x = 0$) to a strongly correlated Dirac metal ($x = 1$) with possible Mott-Hubbard metal-insulator transitions, charge ordering, ferromagnetism, or superconducting states.

It is challenging to synthesize electron-doped herbertsmithite directly, as Cu^{1+} will not assume the same distorted octahedral site on the kagome lattice as Cu^{2+} under thermodynamic conditions, and copper(I) hydroxide is thermodynamically unstable towards disproportionation and evolution of hydrogen gas. By using low-temperature topochemical techniques, this problem is circumvented by producing a kinetically metastable phase [11–14]. Here, we use intercalation of lithium to produce electron-doped herbertsmithite, $ZnLi_xCu_3(OH)_6Cl_2$, with $0 \le x \le 1.8$.

Laboratory x-ray powder diffraction (XRPD), Fig. 1(b), shows that the underlying structure is maintained throughout the doped series. Lithium is not directly detected due to its small x-ray scattering intensity relative to copper and zinc. Any changes in the lattice parameters as a function of doping are small and are within the resolution of the laboratory x-ray diffractometer (see Supplemental Material (SM) [15]). During Rietveld analysis, CuO and Cu_2O are tested and are absent from the air-free samples by both XRPD and neutron diffraction. Unlike the air-stable parent, the doped samples decompose readily in air, Fig. 1(c), with the most heavily doped samples completely decomposing within hours. This rapid and total decomposition is in agreement with the formation of a reduced copper (Cu^{1+}) hydroxide in the bulk that is prone to decomposition in moisture. The color change from blue to black is also in agreement. As soon as there are any Cu^{1+} ions present, there is another possible optical absorption mode: intervalence charge transfer (i.e., $Cu^{2+} + Cu^{1+} \rightarrow Cu^{1+} + Cu^{2+}$), or, put another way, a transition from an impurity band in the gap to the conduction band. Such absorption modes are common in mixed valent systems, such as the Cu^{1+}–Cu^{2+} mixed valence $(N_2H_5)_2Cu_3Cl_6$ [16].

---

[*] mcqueen@jhu.edu

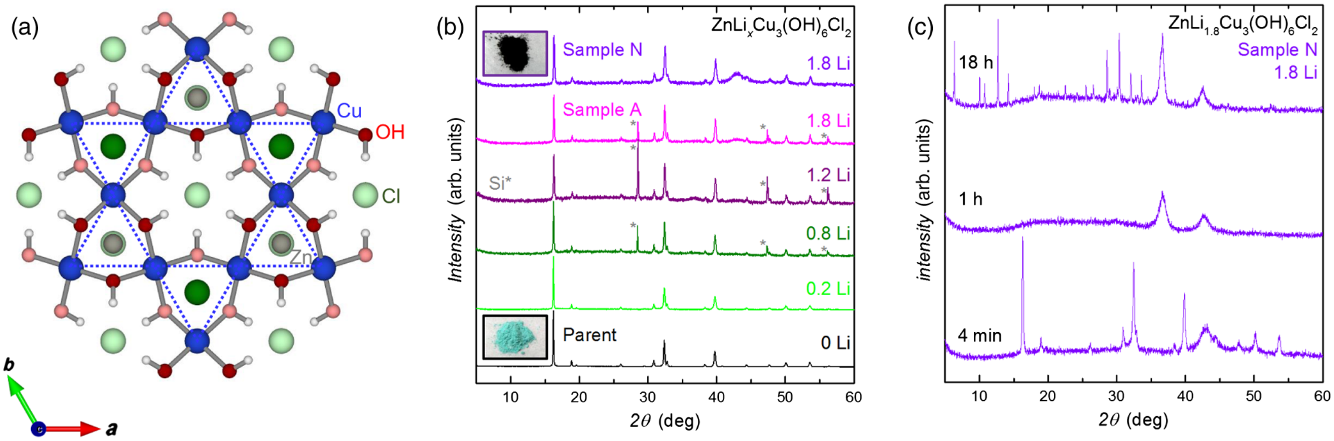

FIG. 1. Doped herbertsmithite structure. (a) A top-down (along c axis) representation of the parent herbertsmithite copper kagome layer (blue dotted line) with Cu (blue) and O (red), H (white), Zn (gray), and Cl (green) between the kagome layers. The dark and light atoms are located above and below the kagome plane, respectively. (b) The x-ray powder diffraction (XRPD) patterns of the complete series. The gray asterisks represent the presence of Si (internal standard). An image of the blue-green parent material is shown in the lower left-hand corner while a picture of the black doped sample N is shown in the upper left. All doped samples are also black. (c) XRPD data demonstrate the instability of one of the maximally doped samples, sample N, in air ($x = 1.8$) as it decomposes in hours into several other phases.

To determine the position of Li within the structure, we carry out neutron powder diffraction of the undoped and maximally Li-doped specimens using the high-flux NOMAD diffractometer at the Spallation Neutron Source, Oak Ridge National Laboratory (see SM [15]). Rietveld analysis reveals that the previously reported structure accurately models the data of the doped specimens, with the exception of the presence of a pocket of negative scattering in a tetrahedral hole formed by three (OH^-) and one Cl^- group, located above and below the copper triangles in the kagome layer. This is consistent with the presence of Li, which has a negative scattering factor. Although the site is physically small for a Li ion, the connectivity is consistent with a favorable tetrahedral bonding environment for Li. The XRPD studies are also consistent with this model. There are systematic changes in the O-Cu-Cl bond angle and the O-Cu, Cl-Cu, and O-O bond lengths (see SM [15]). As the doping increases, the oxygen atoms move away from the Cu kagome lattice and spread from one another. In concert, the Cl atom moves away from the kagome lattice along the c axis. These combined movements create more space in the Cl-$(OH)_3$ tetrahedral hole. Further, a similar geometry is found in $CuMg_2Li_{0.31}$ [17], and a stable Rietveld refinement is obtained for the maximally doped sample N, when including Li in that site, with the occupancy refining to ~0.9 [$x = 1.8(3)$ per formula unit; see SM [15]]. This structure puts the Li ion in close proximity to the Cl atom and appears to form a neutral LiCl dimer along the c axis with a bond distance of ~1.4 Å. Such a dimer is consistent with our attempts to intercalate the larger K^+ ion, which results instead in the formation of KCl. Future work is needed to determine if this model is an accurate description of the local atomic structure.

X-ray photoelectron spectroscopy (XPS) provides a direct probe of the chemical environment of copper and is carried out on the parent and two maximally doped specimens, A and N. The results are consistent with the reduction of Cu^{2+} to Cu^{1+}. Firstly, the four peaks in the parent Cu $2p$ envelope, Fig. 2(a), are indicative of the two final states in divalent copper, (i) the $3d^{10}L^{-1}$ due to an exiting photoelectron leaving a core hole causing a charge transfer process between the surrounding ligands and Cu d shell and (ii) the $3d^9L$ satellite. In the doped samples, this satellite is greatly reduced due to the filled $3d$ shell in Cu^{1+} preventing this loss transition from occurring [19,20]. If it were purely a Robin-Day class 1 mixed valance (pure Cu^{1+} and Cu^{2+} sites with no interactions of ground or excited states), we would expect a mixed XPS signal of Cu^{1+} and Cu^{2+} with an approximate 2∶1 ratio. In this case, however, there must be interactions between neighboring Cu^{1+} and Cu^{2+}, given the shared hydroxyl bridge, through which we know (from the parent) that adjacent Cu ions interact [21–23]. The result is a suppression of the Cu^{2+} XPS satellites, even though resistance measurements show the charges must be localized. This model (which has discrete Cu^{1+} and Cu^{2+} ions, Robin-Day class 2) would not only suppress the Cu^{2+} satellites but also give rise to an optical intervalence charge transfer, which would explain the black color of the material upon even light doping.

Secondly, the photoelectron-induced Auger Cu $L_3M_{4,5}M_{4,5}$ spectra, Fig. 2(b), of the maximally doped specimens are in between and distinct from the $L_3M_{4,5}M_{4,5}$ spectra of the Cu foil and the parent herbertsmithite. Further, a Wagner plot analysis, Fig. 2(c), shows that the Li-doped samples are in a distinctly different chemical environment than either the parent (fully Cu^{2+}) or Cu metal (fully Cu^0) [24], consistent with the structure suggested by our neutron diffraction studies and indicative of the

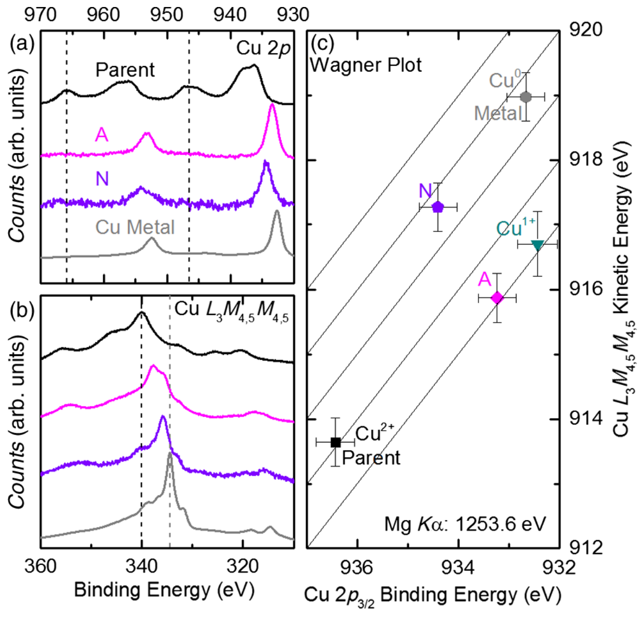

FIG. 2. X-ray photoelectron spectroscopy (XPS). (a) Cu $2p$ XP spectra of parent herbertsmithite (black), sample A (magenta), sample N (violet), and Cu metal (gray). The black dashed line indicates locations of satellite peaks in the parent, characteristic of Cu^{2+}, which are significantly reduced in the doped samples. (b) The x-ray generated Auger Cu $L_3M_{4,5}M_{4,5}$ spectra of the same four samples. The black and the gray dotted lines represent the location of the greatest intensity peak for the parent and the copper metal, respectively. The peak shape and binding energy of the doped samples varies significantly from both the parent and the copper metal. (c) A Wagner plot shows the relative chemical shift of the four samples and Cu^{1+} in $Cu(I)_2O$ (literature value) [18] by plotting the kinetic energy from the Cu $L_3M_{4,5}M_{4,5}$ peak on the y axis and the binding energy from the Cu $2p_{3/2}$ peak on the x axis. The chemical shift is sensitive to the polarizability of the chemical environment.

presence of Cu^{1+} [19,20]. Although information on copper oxidation states is lost in a depth profile analysis with ion sputtering, it can be used to determine the chemical composition [25]. As expected from the topochemical synthesis method, a thin surface layer of Li and benzophenone starting material is detected; upon ion sputtering (up to 100 min), the ratio of Cu : Zn : Cl is in agreement with the expected parent herbertsmithite phase, with Li located throughout (see SM [15]).

Despite the introduction of a substantial number of electrons, the material remains insulating: two probe room temperature resistance measurements on cold-pressed pellets in a glovebox give a resistance > 2 MΩ for the doped series. Figure 3(a) shows the magnetic susceptibility, $\chi \approx M/H$, for the $ZnLi_xCu_3(OH)_6Cl_2$ series. For $x = 0$, the inverse magnetic susceptibility is well known to be linear at high temperatures and dominated by the kagome network, with the signal at $T < 20$ K containing significant contributions from defect Cu^{2+} ions on the Zn^{2+} site between kagome layers [5]. We thus perform fits to the Curie-Weiss law in the low-temperature ($T = 1.8$–15 K) and high-temperature ($T = 100$–300 K) regions to extract estimates of the number of spins arising from the intrinsic and excess Cu ions, respectively, as a function of x. The extracted Curie constants of both the low- and high-temperature regions decrease linearly with increasing doping level, Fig. 4(a). This systematic decrease is consistent with the reduction of magnetic Cu^{2+} ($S = 1/2$) to nonmagnetic Cu^{1+} ($S = 0$). With an x-intercept value of $x = 3.3(5)$, the high-temperature extrapolation to zero is also consistent with the known stoichiometry of herbertsmithite, $Zn_{0.85}Cu_{3.15}(OH)_6Cl_2$, where $x = 3.15$ would be necessary to convert all Cu^{2+} to Cu^{1+}. All of the Weiss temperatures are negative, becoming less negative upon doping (see SM [15]), in agreement with the expectation that the number of spins is reduced in the lattice. The low-temperature extrapolation x-intercept value is $x = 3.9(9)$; this is within error equal to that found from the high-temperature extrapolation. Any subtle divergence between the high- and low-temperature x intercept likely reflects a difference in reducibility of the kagome compared to the interlayer Cu^{2+} ions, since the high-temperature paramagnetism includes both the kagome and interlayer spins, whereas the latter is attributable only to the interlayer defect spins. Given the placement of the Li ions near the kagome layer, it is no surprise the kagome layers are more greatly reduced than the interlayer sites. Further, the difference in local coordination (interlayer Cu in O_6 octahedron versus kagome Cu in O_4Cl_2 octahedron) would result in a difference in redox potential for $Cu^{2+} + e^- \rightarrow Cu^{1+}$ between the two sites, so reducing one should be slightly more favorable than reducing the other.

Figure 3(b) shows the low-temperature heat capacity. There are two regions of significant entropy change as a function of doping: at $T \approx 5$ K, the heat capacity of the sample decreases with increasing Li content, while at higher temperatures there is an entropy gain at nonzero x. Qualitatively, the low-temperature data can be explained by the same mechanism as the magnetization, namely, a reduction of the number of spins as Cu^{2+} is converted to Cu^{1+}. To more quantitatively describe the changes, we parametrize the temperature-dependent data as a function of composition and apply magnetic field with the model:

$$C_p = \gamma T + \beta_3 T^3 + \beta_5 T^5 + A_{\mathrm{LT}} f(\Delta_{\mathrm{LT}}, T) + A_{\mathrm{HT}} f(\Delta_{\mathrm{HT}}, T), \tag{1}$$

$$Af(\Delta, T) = AR(\Delta/T)^2 \frac{e^{\Delta/T}}{(1 + e^{\Delta/T})^2}. \tag{2}$$

The γT term captures the linear contribution to the specific heat from the spin liquid (either intrinsic or due to defect spins). The phonon contribution is described by the $\beta_3 T^3$ and $\beta_5 T^5$ terms [26]. These phonon terms are calculated

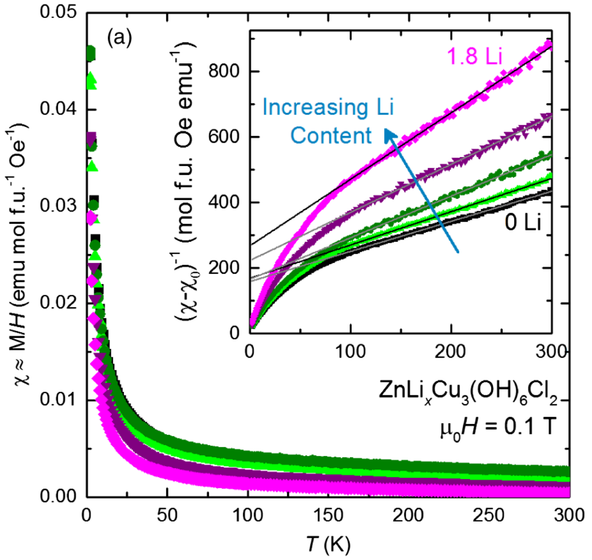

FIG. 3. Physical properties of $\mathrm{ZnLi}_x\mathrm{Cu}_3(\mathrm{OH})_6\mathrm{Cl}_2$ series. (a) The magnetic susceptibility, $\chi \approx M/H$, as a function of temperature for the doped $\mathrm{ZnLi}_x\mathrm{Cu}_3(\mathrm{OH})_6\mathrm{Cl}_2$ series. Black and gray lines are from high-temperature Curie-Weiss analysis of the χ_0-corrected inverse magnetic susceptibility (inset). All samples have paramagnetic behavior and a decrease in susceptibility is seen as Li content increases. (b) Heat capacity divided by temperature as a function of temperature under zero field from $T = 1.8$–20 K. The low-temperature region systematically decreases with increasing Li content across the series, while at higher temperatures the doped samples have increased entropy. Black and gray lines represent fits to the data.

based on the field fit to the parent. The terms are then held constant for the remaining series at $\beta_3 = 4.66(1) \times 10^{-4}$ and $\beta_5 = 4.45(1) \times 10^{-7}\,\mathrm{J\,K^{-6}\,mol^{-1}}$, respectively. A two-level Schottky anomaly, $A_{\mathrm{LT}} f(\Delta_{\mathrm{LT}}, T)$, where A_{LT} is the scaling factor that determines the peak intensity and Δ_{LT} is the size of the gap, accounts for the contribution from defect spins from interlayer Cu^{2+}. A second two-level Schottky anomaly, $A_{\mathrm{HT}} f(\Delta_{\mathrm{HT}}, T)$, describes the high-temperature features. To reduce the number of independent parameters, the phonon contributions are held fixed across all refinements, as the inserted lithium should result in high-frequency modes with only small perturbations of the low-temperature phonon spectrum. Further, in initial fits, the magnitude of the gap, $\Delta_{\mathrm{HT}} = 73$ K ($T_m = 31$ K), of the high-temperature Schottky anomaly is found to not vary significantly and is thus held constant. Results from the final refinements are given in the SM [15]. While we caution against overinterpretation of many of the obtained values, the magnitude of the high-temperature Schottky anomaly A_{HT} is robust; this is checked by comparing the predictions from fits up to $T = 20$ K to the data extending up to $T = 300$ K in Fig. 5(a). Upon doping, A_{HT} [Fig. 4(b)] sharply increases then begins to gradually decrease.

This model also fits to the field-dependent heat capacity, shown in Fig. 5(b). Similar to the zero-field data, the phonon terms $\beta_3 T^3$ and $\beta_5 T^5$ are calculated based on the field fit to the parent and held constant at the above values for the remaining series. The parameters γ, A_{HT}, and Δ_{HT}

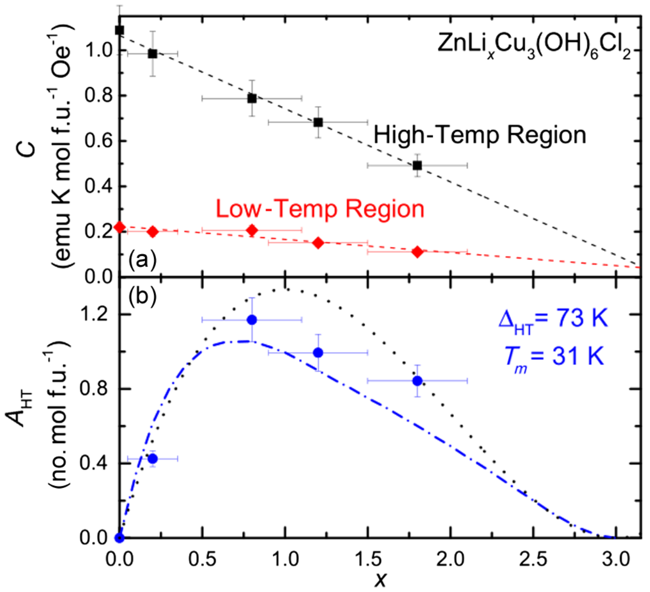

FIG. 4. Magnetization and heat capacity fit parameters. (a) The extracted Curie constants C from the high-temperature (black squares) and low-temperature (red diamonds) Curie-Weiss analysis of the $\mathrm{ZnLi}_x\mathrm{Cu}_3(\mathrm{OH})_6\mathrm{Cl}_2$ series. The dashed lines are a guide to the eye that demonstrate a linear decrease. (b) The Schottky anomaly parameter A_{HT} (blue circles) from heat capacity fits to the doped herbertsmithite series, which describes the feature in the high-temperature heat capacity data. The blue dashed line and the black dotted line are two different models for singlet trapping in doped herbertsmithite (see SM [15]).

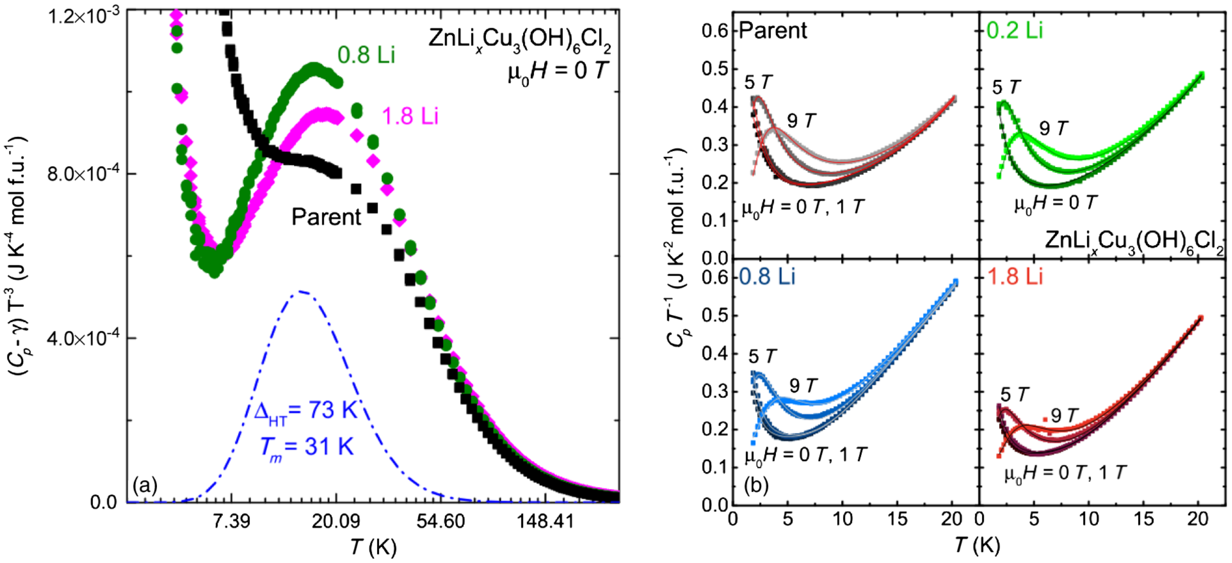

FIG. 5. Detailed heat capacity analysis of $\mathrm{ZnLi}_x\mathrm{Cu}_3(\mathrm{OH})_6\mathrm{Cl}_2$ series. (a) High-temperature $(C_p-\gamma)\,T^{-3}$ Schottky analysis of the temperature range $T = 1.8$–300 K for the parent $\mathrm{ZnCu}_3(\mathrm{OH})_6\mathrm{Cl}_2$ (black), $\mathrm{ZnLi}_{0.8}\mathrm{Cu}_3(\mathrm{OH})_6\mathrm{Cl}_2$ (dark green), and $\mathrm{ZnLi}_{0.8}\mathrm{Cu}_3(\mathrm{OH})_6\mathrm{Cl}_2$ (magenta). The dashed blue line is the high-temperature Schottky anomaly of the extracted values from the zero-field $T = 1.8$–20 K fits. It does a good job of describing the Schottky anomaly we see in the doped samples in the higher-temperature region of the heat capacity. Debye modes (which are a constant at low temperature and fall off at higher temperatures) are not shown for clarity. (b) Simple model fits to field-dependent heat capacity measurements. Top left: the parent $\mathrm{ZnCu}_3(\mathrm{OH})_6\mathrm{Cl}_2$ (black); top right: $\mathrm{ZnLi}_{0.2}\mathrm{Cu}_3(\mathrm{OH})_6\mathrm{Cl}_2$ (green); bottom left: $\mathrm{ZnLi}_{0.8}\mathrm{Cu}_3(\mathrm{OH})_6\mathrm{Cl}_2$ (blue); bottom right: $\mathrm{ZnLi}_{1.2}\mathrm{Cu}_3(\mathrm{OH})_6\mathrm{Cl}_2$ (red). The data sets go from a dark color at low fields to a lighter color at higher fields. The lines are fits as described in the text.

are shared across fields for each sample, and each sample is refined independently until convergence. These constraints yield results consistent with the zero-field fits. All the fits clearly demonstrate the field dependence of the low-temperature feature, which is consistent with a contribution from the magnetic interlayer Cu^{2+}. The low-temperature magnetization measurements, sensitive to the interlayer Cu on the Zn site, indicate that these interlayer Cu atoms are also systematically reduced as a function of doping. If these Cu impurities give rise to the finite γ, it is expected that γ would also be reduced with doping, as observed. Alternately, if the γT term describes the spin-liquid contribution to the heat capacity, a systematic decrease in this value could be explained by the reduction of the spin-liquid nature of the material as electrons are introduced into the system. More interestingly, the high-temperature Schottky anomaly shows no field dependence and reproduces the trend seen in the zero-field data. Direct assignment of the heat capacity terms to specific origins is future work, but it is promising that a single model recapitulates data across temperatures, fields, and composition.

These experimental data are in good agreement with two models for singlet trapping as a function of doping: a Monte Carlo simulation of the trapping of neighboring singlets by Cu^{1+} defects [blue dashed line Fig. 4(b)] and a calculation of singlet trapping by localized electrons on Cu triangles in the kagome lattice (black dotted line) (see SM [15]). Since the magnitude of the gap is on the same order as the expected singlet-triplet gap energy in isolated valence bonds in herbertsmithite [27], it is alluring to interpret the growth in high-temperature specific heat as arising due to the trapping of valence bonds into a glass or solidlike state. However, further work is needed to exclude other possibilities, such as a localized oscillator mode arising from the inserted Li ions. The singlet trapping models are also in agreement with the magnetization data. Every intercalated Li atom reduces one Cu atom, removing its spin contribution and yielding a one-to-one relationship. So upon doping, the Curie constant will linearly go to zero, in agreement with the experimental data.

In conclusion, we successfully introduce electrons into the prototypical kagome quantum spin-liquid herbertsmithite. Despite the predictions, the doping of this system does not lead to metallicity or superconductivity down to $T = 1.8$ K. The magnetic field, temperature, and composition-dependent specific heat all fit remarkably well to a single model. What are the precise physical origins responsible for this behavior? It is plausible that the location of the inserted Li ions provides a sufficiently strong disorder potential that Anderson localization is never overcome, irrespective of electron count, but other explanations cannot be ruled out [28,29]. The interesting physics is the following: Why does charge doping this spin liquid not change it into a metal? The lower connectivity, i.e., the

2D kagome lattice connects to four magnetic neighbors ($n = 4$) as compared to six magnetic neighbors of a 2D triangular lattice ($n = 6$), may also play a role in the doped series behavior. Previous pressure and doping studies on higher connectivity frustrated geometries, such as organic triangular lattice κ-$(ET)_2Cu_2(CN)_3$ [30], Na_xCoO_2 [31], and $Na_4Ir_3O_8$ [32,33], display metallicity. However, to our knowledge, no one has successfully induced metallic behavior in lower connectivity magnetically frustrated structures such as the kagome ($n = 4$) or honeycomb lattice ($n = 3$). And finally, what is the nature of the ground state of doped herbertsmithite? Our results demonstrate the need for an improved approach to describe and predict how electron doping affects magnetically frustrated narrow band insulators and implies that, if metallicity is to be induced, the doping method must involve chemical changes far from the kagome layers.

This work was supported by the NSF, Division of Materials Research (DMR), Solid State Chemistry (SSMC), CAREER grant under Award No. DMR-1253562, and the David and Lucile Packard Foundation. T. M. M. was supported by the Institute for Quantum Matter, under Grant No. DE-FG02- 08ER46544. This research used resources at the Spallation Neutron Source, a DOE Office of Science User Facility operated by the Oak Ridge National Laboratory. Z. A. K. acknowledges the assistance of A. Huq and K. Page in collecting powder neutron data from POWGEN and NOMAD/SNS. Z. A. K and T. M. M. also thank H. D. Fairbrother and the Surface Analysis Laboratory in the Department of Material Science and Engineering at The Johns Hopkins University, and O. Tchernyshyov for useful discussions.

APPENDIX: MATERIALS AND METHODS

Phase-pure herbertsmithite is synthesized hydrothermally in a sealed 21-mL acid digestion vessel. Stoichiometric amounts of $ZnCl_2$ and $Cu_2(OH)_2CO_3$ in 10 mL of H_2O are ramped to 210 °C at 60 °C h^{-1}, held for 24 h, and cooled to room temperature at 6 °C h^{-1}. Several batches are made by this process and thoroughly mixed in order to achieve a large supply of the parent material. All further chemical manipulations are done in Schlenk flasks using air-free techniques. Various amounts of Li are added to a 0.20-M benzophenone (Ph_2CO) in THF solution and allowed to stir overnight until all Li dissolves, yielding a deep blue or purple solution depending on Li content. The parent herbertsmithite is then added under the following conditions for the following samples: sample A ($x = 1.8$) is made by intercalation using 1 g of parent material in 50 mL with a molar ratio of 1:1.25 Ph_2CO:Li metal and refluxed for 24 h; sample B ($x = 0.2$) is made by intercalation using 1 g of parent material in 30 mL with a molar ratio of 1.1:1 Ph_2CO:Li metal and heated at 45 °C for 24 h; sample N ($x = 1.8$) is made by intercalation using 3 g of parent material in 200 mL with a molar ratio of 1:1.25 Ph_2CO:Li metal and refluxed for 48 h. 75 mg of sample A ($x = 1.8$) is deintercalated with 15.0 and 25.0 mL of 4.50(2) mM I_2 in acetonitrile at room temperature until the solution becomes clear to create $x = 1.2$ (A2) and $x = 0.8$ (A3) samples, respectively.

Laboratory x-ray powder diffraction patterns are collected using Cu $K\alpha$ radiation ($\lambda = 1.5418$ Å) on a Bruker D8 Focus Diffractometer with a LynxEye detector. Powder neutron diffraction data of sample N at 300 K are collected at the Spallation Neutron Source NOMAD diffractometer (BL-1B) at the Oak Ridge National Laboratory and analyzed with the Rietveld method using GSAS/EXPGUI [34,35]. Compositions of the maximally doped specimens are fixed at the values obtained from NPD; the composition of deintercalated samples is determined by the known quantity of oxidant consumed. All other compositions are estimated based on magnetization data.

X-ray photoelectron spectra are collected using Mg $K\alpha$ radiation (1253.6 eV, 15 kV, 300 W) with a pass energy of 58.7 eV, 0.125 eV/step at 50 ms/step on a PHI 5600 XPS. Select samples are ion sputtered with 4 keV Ar^+ for 5, 15, 60, and 100 min [ion sputter area 6×6 mm^2, target current 1.0(3) μA] with a differential ion gun. XP spectra are energy adjusted to ion sputter cleaned copper metal Cu $2p_{3/2}$ with CasaXPS software. The error in peak position for the Cu $2p$ and Cu $L_3M_{4,5}M_{4,5}$ envelopes is estimated to be ±3 step sizes (0.375 eV).

Magnetization and heat capacity measurements are measured on powders and cold-pressed pellets, respectively, in a Quantum Design Physical Properties Measurement System. Magnetizations are measured from $T = 1.8$–300 K under a field of $\mu_0H = 0.1$ T and susceptibility estimated as $\chi = M/H$. Heat capacity is measured in triplicate at each point using the semiadiabatic pulse technique. Data are collected from $T = 1.8$–300 K under $\mu_0H = 0$ T and from $T = 1.8$–20 K under $\mu_0H = 1, 5, 9$ T. Two probe contact resistivity measurements with a voltmeter on the series of cold-pressed polycrystalline samples at room temperature indicate a resistance of > 2 MΩ.

[1] P. W. Anderson, *Resonating Valence Bonds: A New Kind of Insulator?*, Mater. Res. Bull. **8**, 153 (1973).

[2] P. W. Anderson, *The Resonating Valence Bond State in* La_2CuO_4 *and Superconductivity*, Science **235**, 1196 (1987).

[3] M. Fu, T. Imai, T.-H. Han, and Y. S. Lee, *Evidence for a Gapped Spin-Liquid Ground State in a Kagome Heisenberg Antiferromagnet*, Science **350**, 655 (2015).

[4] L. Balents, *Spin Liquids in Frustrated Magnets*, Nature (London) **464**, 199 (2010).

[5] M. P. Shores, E. A. Nytko, B. M. Bartlett, and D. G. Nocera, *A Structurally Perfect* $S = 1/2$ *Metal-Organic Hybrid Kagomé Antiferromagnet*, J. Am. Chem. Soc. **127**, 13462 (2005).

[6] D. E. Freedman, T. H. Han, A. Prodi, P. Müller, Q.-Z. Huang, Y.-S. Chen, S. M. Webb, Y. S. Lee, T. M. McQueen, and D. G. Nocera, *Site Specific X-Ray Anomalous Dispersion of the Geometrically Frustrated Kagome Magnet, Herbertsmithite,* $\mathrm{ZnCu_3(OH)_6Cl_2}$, J. Am. Chem. Soc. **132**, 16185 (2010).

[7] S. Chu, T. M. McQueen, R. Chisnell, D. E. Freedman, P. Müller, Y. S. Lee, and D. G. Nocera, *A* Cu^{2+} *($S = 1/2$) Kagomé Antiferromagnet:* $\mathrm{Mg}_x\mathrm{Cu}_{4-x}\mathrm{(OH)_6Cl_2}$, J. Am. Chem. Soc. **132**, 5570 (2010).

[8] T.-H. Han, J. S. Helton, S. Chu, D. G. Nocera, J. A. Rodriguez-Rivera, C. Broholm, and Y. S. Lee, *Fractionalized Excitations in the Spin-Liquid State of a Kagome-Lattice Antiferromagnet*, Nature (London) **492**, 406 (2012).

[9] I. I. Mazin, H. O. Jeschke, F. Lechermann, H. Lee, M. Fink, R. Thomale, and R. Valentí, *Theoretical Prediction of a Strongly Correlated Dirac Metal*, Nat. Commun. **5**, 4261 (2014).

[10] D. Guterding, H. O. Jeschke, and R. Valentí, *Prospect of Quantum Anomalous Hall and Quantum Spin Hall Effect in Doped Kagome Lattice Mott Insulators*, Sci. Rep. **6**, 25988 (2016).

[11] M. A. Hayward, E. J. Cussen, J. B. Claridge, M. Bieringer, M. J. Rosseinsky, C. J. Kiely, S. J. Blundell, I. M. Marshall, and F. L. Pratt, *The Hydride Anion in an Extended Transition Metal Oxide Array:* $\mathrm{LaSrCoO_3H_{0.7}}$, Science **295**, 1882 (2002).

[12] Y. Tsujimoto, C. Tassel, N. Hayashi, T. Watanabe, H. Kageyama, K. Yoshimura, M. Takano, M. Ceretti, C. Ritter, and W. Paulus, *Infinite-Layer Iron Oxide with a Square-Planar Coordination*, Nature (London) **450**, 1062 (2007).

[13] M. J. Rosseinsky, D. W. Murphy, R. M. Fleming, R. Tycko, A. P. Ramirez, T. Siegrist, G. Dabbagh, and S. E. Barrett, *Structural and Electronic Properties of Sodium-Intercalated* $\mathrm{C_{60}}$, Nature (London) **356**, 416 (1992).

[14] J. R. Neilson, A. Llobet, A. V. Stier, L. Wu, J. Wen, J. Tao, Y. Zhu, Z. B. Tesanovic, N. P. Armitage, and T. M. McQueen, *Mixed-Valence-Driven Heavy-Fermion Behavior and Superconductivity in* $\mathrm{KNi_2Se_2}$, Phys. Rev. B **86**, 054512 (2012).

[15] See Supplemental Material at http://link.aps.org/supplemental/10.1103/PhysRevX.6.041007 for additional neutron and x-ray powder diffraction refinements and analysis, supplemental x-ray photoelectron spectra, tabulated magnetization and heat capacity values, and proposed singlet trapping/electron localization models.

[16] B. Scott and R. Willett, *Crystal Structure and Electronic Spectroscopy of Bis(hydrazinium) Hexachlorotricuprate(2I, II): A Copper(I)-Copper(II) Mixed-Valence System Exhibiting Intervalence Charge Transfer*, Inorg. Chem. **30**, 110 (1991).

[17] M. H. Braga, J. Ferreira, and L. F. Malheiros, *A Ternary Phase in Cu-Li-Mg System*, J. Alloys Compd. **436**, 278 (2007).

[18] NIST X-Ray Photoelectron Spectroscopy Database Version 4.1, NIST Technical Report, http://srdata.nist.gov/xps/.

[19] N. S. McIntyre and M. G. Cook, *X-Ray Photoelectron Studies on Some Oxides and Hydroxides of Cobalt, Nickel, and Copper*, Anal. Chem. **47**, 2208 (1975).

[20] P. van der Heide, *X-Ray Photoelectron Spectroscopy: An Introduction to Principles and Practices* (Wiley, New York, 2011), p. 125.

[21] M. B. Robin and P. Day, Adv. Inorg. Chem. Radiochem. **10**, 247 (1968).

[22] P. Day, N. S. Hush, and R. J. H. Clark, *Mixed Valence: Origins and Developments*, Phil. Trans. R. Soc. A **366**, 5 (2008).

[23] H. Rupp and U. Weser, *X-Ray Photoelectron Spectroscopy of Copper(II), Copper(I), and Mixed Valence Systems*, Bioinorganic chemistry **6**, 45 (1976).

[24] C. D. Wagner, *Auger Lines in X-Ray Photoelectron Spectrometry*, Anal. Chem. **44**, 967 (1972).

[25] G. Panzner, B. Egert, and H. P. Schmidt, *The Stability of CuO and* $\mathrm{Cu_2O}$ *Surfaces during Argon Sputtering Studied by XPS and AES*, Surf. Sci. Lett. **151**, A83 (1985).

[26] A. Tari, *The Specific Heat of Matter at Low Temperatures* (Imperial College Press, London, 2003).

[27] R. R. P. Singh and D. A. Huse, *Triplet and Singlet Excitations in the Valence Bond Crystal Phase of the Kagome Lattice Heisenberg Model*, Phys. Rev. B **77**, 144415 (2008).

[28] P. W. Anderson, *Absence of Diffusion in Certain Random Lattices*, Phys. Rev. **109**, 1492 (1958).

[29] J. P. Sheckelton, J. R. Neilson, and T. M. McQueen, *Electronic Tunability of the Frustrated Triangular-Lattice Cluster Magnet* $\mathrm{LiZn}_{2-x}\mathrm{Mo_3O_8}$, Mater. Horiz. **2**, 76 (2015).

[30] Y. Kurosaki, Y. Shimizu, K. Miyagawa, K. Kanoda, and G. Saito, *Mott Transition from a Spin Liquid to a Fermi Liquid in the Spin-Frustrated Organic Conductor* $\kappa\text{-}\mathrm{(ET)_2Cu_2(CN)_3}$, Phys. Rev. Lett. **95**, 177001 (2005).

[31] M. Lee, L. Viciu, L. Li, Y. Wang, M. L. Foo, S. Watauchi, R. A. Pascal, R. J. Cava, and N. P. Ong, *Large Enhancement of the Thermopower in* $\mathrm{Na}_x\mathrm{CoO_2}$ *at High Na Doping*, Nat. Mater. **5**, 537 (2006).

[32] Y. Okamoto, M. Nohara, H. Aruga-Katori, and H. Takagi, *Spin-Liquid State in the* $S = 1/2$ *Hyperkagome Antiferromagnet* $\mathrm{Na_4Ir_3O_8}$, Phys. Rev. Lett. **99**, 137207 (2007).

[33] D. Podolsky and Y. B. Kim, *Spin-Orbit Coupling in the Metallic and Spin-Liquid Phases of* $\mathrm{Na_4Ir_3O_8}$, Phys. Rev. B **83**, 054401 (2011).

[34] A. C. Larson and R. B. Von Dreele, *General Structure Analysis System (GSAS)*, Los Alamos National Laboratory Report No. LAUR 86-748 (2000), https://www.ncnr.nist.gov/xtal/software/gsas.html.

[35] B. H. Toby, *EXPGUI, A Graphical User Interface for GSAS*, J. Appl. Crystallogr. **34**, 210 (2001).